



DFT study of the structural, electronic, and optical properties of bulk, monolayer, and bilayer Sn-monochalcogenides

Attia Batool^a, Youqi Zhu^a, Xilan Ma^a, Muhammad Imran Saleem^b, Chuanbao Cao^{a,*}

^a Research Center of Materials Science, Beijing Key Laboratory of Construction Tailorable Advanced Functional Materials and Green Applications, Beijing Institute of Technology, Beijing, 100081, P. R. China.

^b Department of Materials Science and Engineering, 3D Convergence Center, Inha University, Incheon, 22212, Republic of Korea



ARTICLE INFO

Keywords:
DFT Calculation
CASTEP
Monochalcogenides
Electronic
Optical Properties

ABSTRACT

Tin monochalcogenides (SnSe, SnS), with advantages of earth abundance, environmental friendly, chemical stability, and less toxicity can be used in Li-ion batteries, piezoelectric, optoelectronics, sensors, and thermoelectric. Here, we used the ultra-soft pseudo-potential technique depending on density functional theory with generalized gradient approximation (GGA) to calculate the electronic, optical, and structural properties by changes related to the reduction of dimensionality from bulk to monolayer or bilayer structure. The calculated parameters show that the bandgap energies of SnS and SnSe semiconductors (0.5~1.25 eV) cover the broadband range, and their static dielectric constant confirms the isotropic nature. We compare our theoretical results of different approximations with previously reported DFT-based and experimental results. The calculations of tin monochalcogenides show that as thickness increases, isotropic behavior increases, and material becomes crystalline. This method opens a new window to deeply understand monochalcogenide's structural, optical, and electronic properties for numerous applications, like thermoelectric, photovoltaic, and energy storage devices.

1. Introduction

The enormous properties of graphene have allowed the exploration of new two-dimensional (2D) atomic layered systems for future nanotechnology devices [1–4]. Subsequently, novel 2D materials have been projected and synthesized. Such as II-VIA group element, group III-VA, group V-VA [5–9], MXenes [10–12], 2D-metal oxides [13,14] and transition metal dichalcogenides (TMDs) [15–18]. The layer-controlled direct bandgap nature, higher carrier mobility, and exclusive in-plane anisotropy are the notable features of these 2D materials that make them a rising contender for future thermoelectric applications. Thus, tremendous research efforts have been conducted to investigate the remarkable properties of 2D materials. However, research is still in a growing phase [19].

Further, 2D IV-VI group compounds are also essential for energy storage and conversion devices [20–22]. Among them tin monochalcogenides (Sn-monochalcogenides) are well-known 2D semiconductor. Sn-monochalcogenides are the structural derivatives of orthorhombic black phosphorus that contain a ridged, highly anisotropic structure with an energy gap between 0.5–1.25 eV [23,24]. The condition for a significantly high chemical and ecological balance of SnX

(X=Se, S) is the layers of cations that are separated by van der Waals (vdW) forces [25]. It is currently a rising devotion in the thermoelectric community because of their amazingly high figure of merit (ZT) in p-type single crystals [26–28].

Additionally, Sn-monochalcogenides have extensively been studied in optoelectronic devices, lithium-ion batteries, and catalysis. As compared with toxic lead (Pb) and cadmium (Cd) divalent metals, the power conversion efficiency (PEC) of earth-abundant, non-toxic and inexpensive Sn-monochalcogenides based photovoltaic cells has recently exceeded by 20%, showing the tremendous potential for commercialization [29].

The structural, optical, and electronic properties of 2D Sn-monochalcogenides are widely being explored by using theoretical-based calculations. For example, Gomes et al. conducted the first-principles calculation of structural, optical, and electronic properties of SnX (X=S, Se). They predicted the variations associated with dimensionality by using Kohn-Sham density functional theory (KS-DFT) as implemented in the QUANTUM ESPRESSO code. The calculated bandgap values of the bulk, bilayer, and monolayer of binary semiconducting tin sulfide (SnS) are 1.24, 1.60 and 1.96 eV, respectively. Additionally, the calculated bandgap values of binary semiconducting

* Corresponding author.

E-mail address: cba@bit.edu.cn (C. Cao).

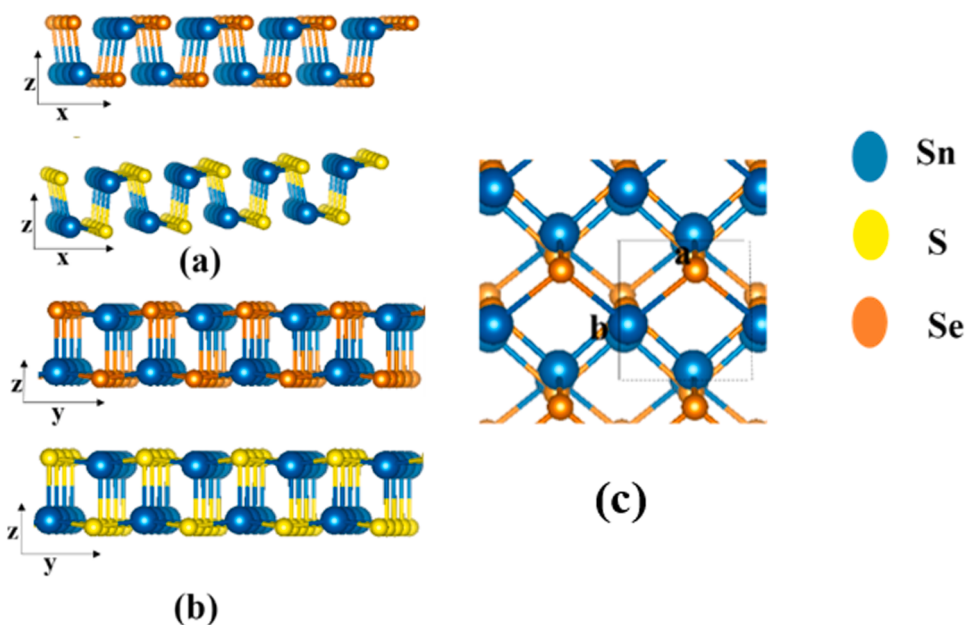


Fig. 1. Optimized geometrical structures of SnSe and SnS: (a) Adjacent view of x-z plane (SnSe, SnS), (b) adjacent views of y-z plane (SnSe, SnS), and (c) upper view of SnSe along the lattice vectors a and b beside x and y directions.

tin selenide (SnSe) of bulk, bilayer, and monolayer are 1.0, 1.20, and 1.51 eV, respectively. It has been observed that the valence and conduction bands have multiple valley structures, later with the spin-orbit splitting of the order of 19–86 meV [25]. Singh et al. conducted the theoretical analysis to describe previously unknown single-layer of monochalcogenides. They predicted that the two-dimensional Sn-mono-chalcogenides were most stable in a highly distorted NaCl-type structure using the projector augmented wave method implemented in the plane-wave code VASP. The acquired bandgap value of SnSe monolayer, bilayer, and bulk are 1.40 eV, 1.20 eV, and 1.0 eV, respectively [30]. Xu et al. described the optical and electronic properties of the monolayer group-IV monochalcogenides with the help of generalized gradient approximation (GGA) of the Perdew-Burke-Ernzerhof (PBE) functional. The calculated carrier mobility ranges $10^{-3}\text{--}10^{-5}$ cm 2 V $^{-1}$ s $^{-1}$ and is highly orientation-dependent [31]. Recently, T. V. Vu et al. studied the SnSe monolayer by DFT calculations using the GGA-PBE approach for XC potential employing the WIEN2k package. SnSe monolayer revealed valence band maximum (VBM) along Γ -X path and two conduction band minima (CBM) along Γ -X and Y- Γ paths. Their result suggests that monolayer SnSe is a quasi-direct-band semiconductor with a bandgap of about 0.9 eV [32]. However, parallel studies on the optical, electronic and structural properties of orthorhombic SnX have seldom been compared and calculated. Thus, in this report, we have used CASTEP software with DFT exchange-correlation contribution GGA through PBE functional to explore optical, electronic, and structural properties. Then, we compare our results by exploiting GGA-PBE. We compare changes in the electronic structure and optical properties from SnX monolayer to bilayer and, then, to bulk material. The calculated structural, electronic, and optical values are comparable with previously reported experimental ones. Theoretically, our calculation predicts that the SnX has tunable optoelectronic properties, which can vary by changing thickness from three-dimensional to two-dimensional. Thus, this work will pave the way to understanding the peculiar properties of variation associated with the dimensionality of Sn-monochalcogenides with GGA-PBE approximation.

2. Computational detail

Structural moderation and electronic calculation are obtained by

density functional theory (DFT) as fulfilled in the Cambridge Serial Total Energy Package CASTEP [33]. The DFT exchange-correlation contribution is calculated using the GGA through PBE functional [34]. Ultra-soft pseudo-potentials are used for the electrostatic interactions among ionic cores and valence electrons. Density mixing is used for the electronic structure, and Broyden-Fletcher-Goldfarb-Shanno (BFGS) geometry optimization has improved the indicated symmetry of crystal structure [35]. The subsequent electronic orbitals are used for SnSe and SnS are (Sn 5s 2 5p 2 , Se 4s 2 4p 4 , S 3s 2 3p 4) to develop the conduction and the valence bands. The total energy of all optimize cells can be concluded from periodic boundary conditions. On a plane wave basis, the trial wave functions are expanded.

The cut-off energy for the plane wave expansion is taken as 280 eV k-point sampling within the Brillouin-zone (BZ). In Monkhorst-Pack grid scheme for the compound under study has been conceded out with $2 \times 3 \times 1$ special points [36]. This confirms the convergence of the energy cell volume calculations. Geometry optimization is completed using the self-consistent convergence thresholds of 5×10^{-6} eV atom $^{-1}$ for the total energy, 5×10^{-4} Å for maximum displacement, 0.02 GPa for maximum stress, and 0.01 eV Å $^{-1}$ for the maximum force. We used periodic boundary conditions along the three dimensions for monolayer and bilayer models. We applied vacuum regions of 15 Å between adjacent images in the path perpendicular to the layers—convergence checks with larger vacuum spacing assurance to avoid false interaction between adjacent images.

3. Result and Discussion

Fig. 1(a)-b illustrates the optimized crystal structures of monolayer SnX (X=S, Se). The orthorhombic structure of SnX (X=Se, S) consists of eight atoms per primitive unit cell in the bulk alpha phase. In SnX (X=Se, S), the primitive unit cell comprises two wrinkled layers arranged on top of each other. The bilayer structure of Sn-monochalcogenides is obtained by increasing the lattice super-cell vector thickness perpendicular to the layer plane. **Fig. 1(c)** shows that the monolayer has four atoms per unit cell. The zigzag rows of alternating elements are formed so that each atomic species is covalently bonded to three neighbors of the other atomic species. Consequently, a lone pair in each atom pushes its three bonds towards tetrahedral coordination.

Table 1

Optimized lattice parameters for Sn-monochalcogenides (monolayer, bilayer, and bulk) all values are given in Å unit.

Material	Monolayer		Bilayer		Bulk		
	a	b	a	b	a	b	c
SnSe	4.36	4.25	4.42	4.30	4.46	4.19	11.57
SnS	4.22	3.98	4.26	4.04	4.34	4.01	11.82

(Note: a, b, c denote lattice parameters).

SnX ($X=\text{S}, \text{Se}$) belongs to the class of layer materials with an orthorhombic crystal arrangement and analogous hinge-like structure along the armchair direction. Astonishingly, this is a distinctive property in distorted silicone and graphene. Due to the similar electronegativity and analogous bond strengths of Se, S, and Sn, the lattice parameters show little variation among the two compounds differing by less than 7%. The lattice parameters of the selenides show little variations of $\sim\pm 2\%$, while those of sulfides remain nearly unchanged for a different number of layers [37,38]. The calculated lattice parameters for bulk SnSe ($a = 4.46 \text{ \AA}$, $b = 4.19 \text{ \AA}$, and $c = 11.57 \text{ \AA}$) [35] and for bulk SnS ($a = 4.22 \text{ \AA}$, $b = 3.98 \text{ \AA}$, and $c = 11.82 \text{ \AA}$) are in good agreement with experimental data (calculated lattice parameter values are illustrated in Table 1) [39,40]. As the materials evolve from three-dimension to two-dimension (monolayer to bilayer), the slight increase in lattice parameters causes the bandgap decreases due to an increase in grain crystal size.

3.1. Electronic properties of monolayer, bilayer, and bulk SnX ($X=\text{S}, \text{Se}$)

The energy and location in the k-space near CBM and VBM are responsible for the bandgap and nature of conversion. The group-IV mono-chalcogenides possess the most exciting properties of a tunable bandgap. The energy-gaps (E_g) values were obtained by calculating the band structures using GGA-PBE approximation along the high symmetry paths of the BZ, as listed in Table 2. The GGA-PBE approximation is carried out on an identical wide range of materials that can relax and expands bonds. Owing to the Sn-5s character of those bands, the dispersion of the bands adjacent to the gap is nearly similar to the F-G and Z-Q directions. Except for the bulk SnSe, most of the compounds (e.g., monolayer and bilayer SnX) have an indirect gap owing to valence-band and conduction-band valleys, as presented by our calculated band structures in Fig. 2. Finally, as expected, with an increasing number of layers (i.e., mono and bilayer), the bandgap decreases due to an increase in grain crystal size.

The calculated electronic band structure of SnSe and SnS (monolayer, bilayer, and bulk) is shown in Fig. 2. From here, the monolayer SnSe has an indirect gap of 1.44 eV, quantified along the F-G line. The bilayer band structure displays slight variations in the bandgap, and bilayer SnSe is categorized by an indirect gap of 0.932 eV, because the VBM and CBM are currently between the F-G lines. In bulk SnSe, the VBM and CBM are along with the Z point, and a direct gap of 0.50 eV is observed. From here, one can see that the calculated direct and indirect gaps of SnSe are comparable with experimentally predictable values of 0.95 and 1.15 eV [41]. Accompanied by GGA-PBE approximation, the

bandgap values of SnS for monolayer, bilayer, and bulk are 1.82 eV, 1.18 eV, and 0.625 eV, which is also comparable with experimentally as well theoretically predicted gap energies reported in the literature [42].

The energy gap measured in optical experiments differs from the conduction gaps due to exciton binding energy. The difference between the GGA-PBE band and experimental band energies in 2D materials is a few hundred meV. Theoretically, the bandgap difference occurs using GW approximation due to the screening effect in the core of d-bands in SnS [43–47]. The excellent agreement between GGA and experimental energies is unexpected.

From Table 2, one can see that layered SnSe and SnS are suitable for optoelectronic devices and solar energy applications. As described, the bandgap of SnX has in the range of 0.5–1.25 eV, efficiently suitable for the infrared light of solar radiation. Except for bulk SnSe, which reveals a direct bandgap, the monolayer and bilayer SnX compounds are indirect bandgap semiconductors. According to Zhang and coworkers, for photocatalytic activity, the indirect bandgap materials are more suitable owing to the recombination of photo-generated electrons being reduced due to the presence of different k-vectors for VBM and CBM [48].

3.2. Optical properties

The GGA-PBE approximation calculation is carried out to understand the light-matter interaction and optical properties of Sn-monochalcogenides, as illustrated in Fig. 3. Considering the significance of lower dimensionality and the influence of anisotropy, the optical properties can mathematically be described by a complex dielectric function $\epsilon(\omega)$; which is expressed as follows $\epsilon(\omega)=\epsilon_1(\omega)+i\epsilon_2(\omega)$, where $\epsilon_1(\omega)$ and $\epsilon_2(\omega)$ symbolize the real and imaginary parts associated with the band structure. It can be calculated by considering all transitions between occupied and unoccupied electronic states. The Kramers-Kronig transformation is used to relate the real and imaginary parts. It is also used to calculate the function of the real part from the imaginary.

To calculate optical constants like absorption coefficient (α), optical conductivity (σ), and refractive index (n), the following 1–8 equations are used [50,51]

Where ω represents the light frequency, u symbolizes the incident electric field polarization, Ψ_k^v and Ψ_k^c represent the functions of the valence and conduction bands at k , e and P show the electric charge and principal values.

$$\epsilon_1(\omega) = 1 + \frac{2}{\pi} P \int_0^\infty \frac{\omega' \epsilon_2(\omega')}{\omega'^2 - \omega^2} d\omega' \quad (1)$$

$$\epsilon_2(\omega) = \frac{2e^2 2\pi}{\Omega \epsilon_0} \sum_{k,v,c} |\Psi_k^c| u.r |\Psi_k^v| \delta(E_k^c - E_k^v - \omega) \quad (2)$$

$$n(\omega) = \frac{\sqrt{2}}{2} \left[\sqrt{\epsilon_1^2(\omega) + \epsilon_2^2(\omega)} + \epsilon_1(\omega) \right]^{\frac{1}{2}} \quad (3)$$

$$k(\omega) = -\frac{\sqrt{2}}{2} \left[\sqrt{\epsilon_1^2(\omega) + \epsilon_2^2(\omega)} + \epsilon_1(\omega) \right]^{\frac{1}{2}} \quad (4)$$

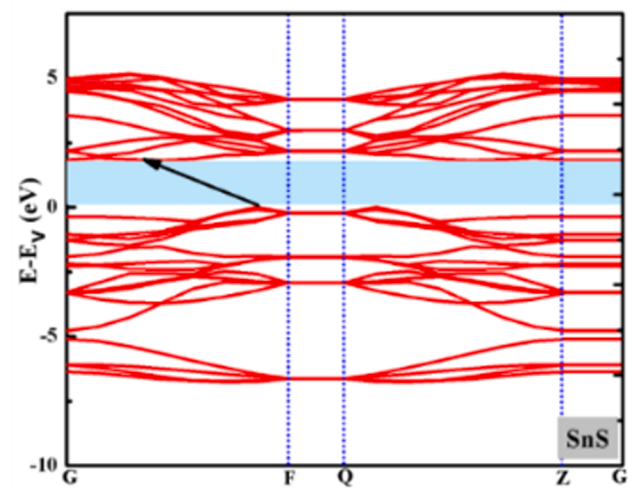
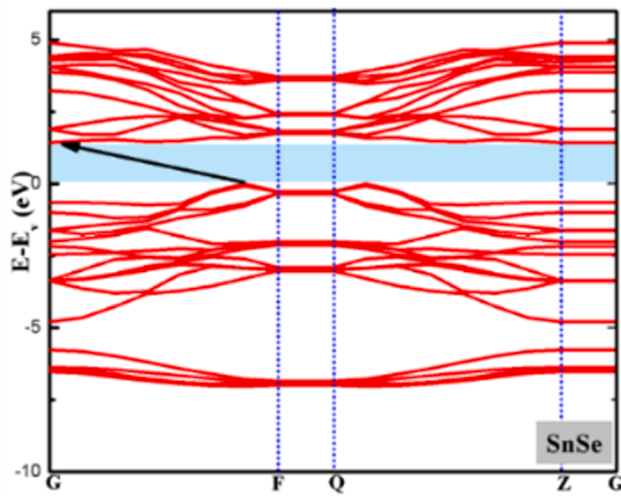
Table 2

Bandgap energies calculations for Sn-monochalcogenides (monolayer, bilayer, and bulk). We compare results from VASP code, Quantum Espresso (QE), WIEN2K and our calculated results using the GGA-PBE approach. Experimental results from previous literature are also shown.

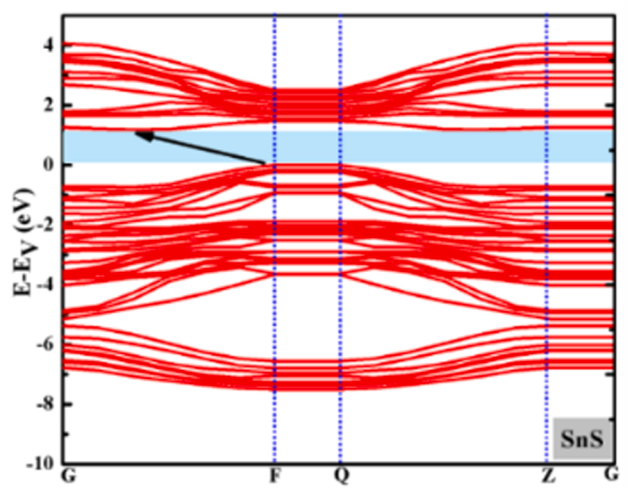
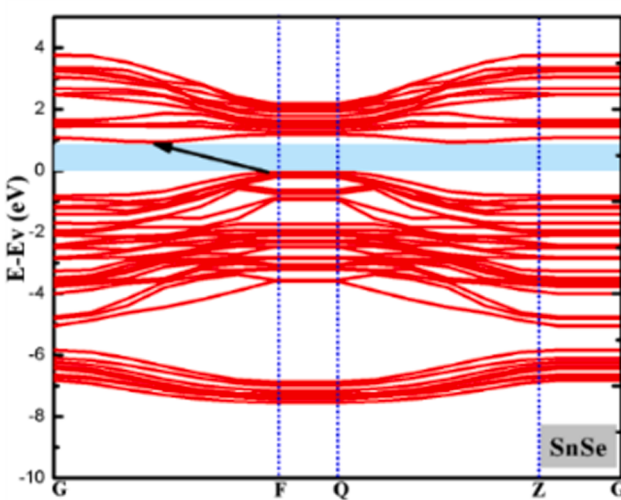
	Monolayer*					Bilayer*					Bulk*					Experiment
	GGA-VASP	GGA-QE	HSE-VASP	GGA-PBE WIEN2k	GGA-PBE CASTEP	GGA-VASP	GGA-QE	HSE-VASP	GGA-PBE CASTEP	GGA-VASP	GGA-QE	HSE-VASP	GGA-PBE CASTEP	Experiment		
SnSe	0.96	1.01	1.44	0.9 [32]	1.44 (Our results)	0.76	0.79	1.20	0.93 (Our results)	0.54	0.55	1.00	0.50 (Our results)	0.95–0.89 [41, 49]		
SnS	1.38	1.40	1.96	-	1.82 (Our results)	1.12	1.14	1.60	1.18 (Our results)	0.82	0.83	1.24	0.62 (Our results)	1.20–1.37 [42]		

(* Note: Here bandgap values are measured in eV).

Monolayer



Bilayer



Bulk

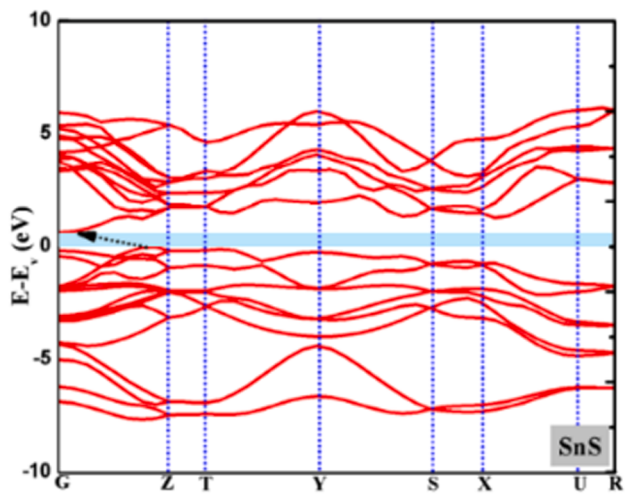
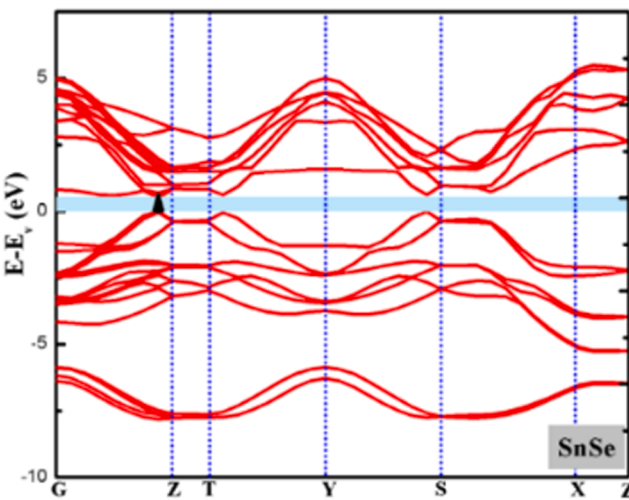


Fig. 2. Calculated electronic band structure of SnSe and SnS (monolayer, bilayer and bulk) using the GGA-PBE functional.

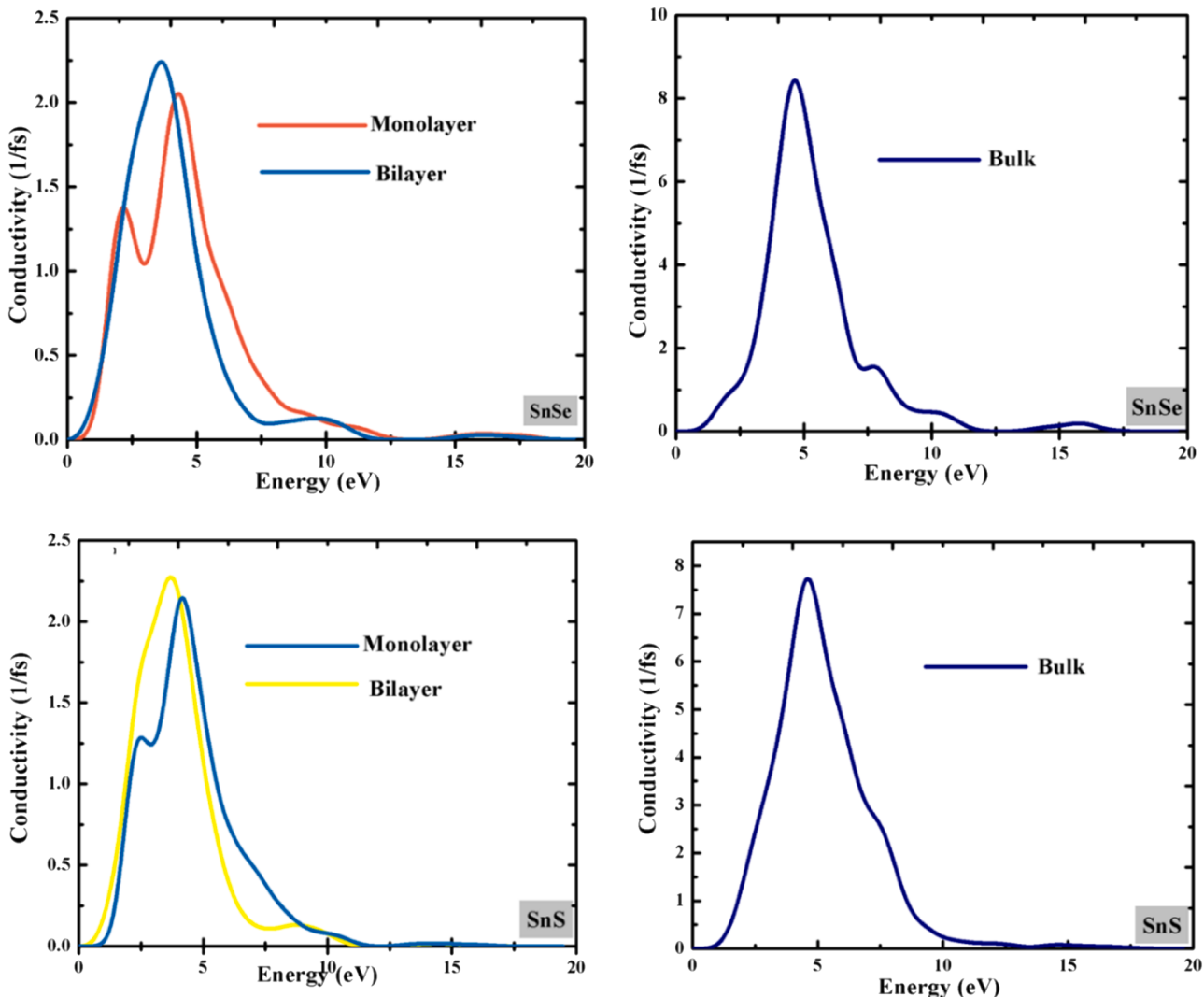


Fig. 3. Comparison of the real part of conductivity of SnSe, SnS (monolayer, bilayer) with their bulk form.

$$\alpha(\omega) = \sqrt{2} \left[\sqrt{\epsilon_1^2(\omega) + \epsilon_2^2(\omega)} - \epsilon_1(\omega) \right]^{\frac{1}{2}} \quad (5)$$

$$\sigma(\omega) = \operatorname{Re} \left(-i \frac{\omega}{4\pi} (\epsilon(\omega) - 1) \right) \quad (6)$$

$$R(\omega) = \frac{(n-1)^2 + k^2}{(n+1)^2 + k^2} \quad (7)$$

$$L(\omega) = \frac{\epsilon_1(\omega)}{\epsilon_1^2 + \epsilon_2^2(\omega)} \quad (8)$$

Fig. 3 compares the real part of conductivity “ $\sigma(\omega)$ ” acquired for monolayer, bilayer, and bulk Sn-monochalcogenides. From here, one can see the overall symmetrical behavior of both materials (SnSe, SnS). The highest peak in the real part of $\sigma(\omega)$ is slightly above the absorption edge corresponding to a band nesting region. The conductivity $\sigma(\omega)$ for monolayer, bilayer, and bulk shows a distinct and prominent peak then immediately reduced to zero eV. For SnSe (monolayer, bilayer), the first peak appears at 2.1 eV; after that, it reduces quickly and then increases again at 4.3 eV. For SnSe, the optical conductivity can also be detected at 10.00 eV and 16.27 eV, then a flat decline occurs, and optical conductivity reaches zero at 19 eV. Similar behavior occurs in SnS (monolayer, bilayer, and bulk) conductivity. The first peak appears at 2.5 eV (comparable to direct transition) then there is a sharp increase up to 4.1 eV.

The conductivity decreases as the energy increases and eventually drops to zero. Because of band-nesting in SnX, as compared with the bulk, the conductivity in mono and bilayer is intense. Sn-monochalcogenides show isotropic behavior in optical conductivity due to the ionic characteristics of bonding. The optical and band structure properties are expressed by atomic position. Thus, all properties are approximately similar for both materials. In conduction bands closer to the Fermi energy level, numerous 5p electrons and a minor number of 4p electrons are produced by Sn and (Se, S) state correspondingly.

As shown in Fig. 4, the valence band of lower energy range from -4.0 eV to -1 eV is attributed to contact between Sn-5p and (Se, S)-4p. Conversely, Sn-5s and Sn-5p states interact with (Se, S)-4p states in the upper valence bands, forming antibonding states [52]. At lower energies, these electrons become the cause of optical conductivity.

The absorption coefficient of Sn-monochalcogenides is a measure of the rate of decrease in light intensity, as Fig. 5 shows the highest absorption coefficient peak at 4.26 and 4.63 eV ($1.11 \times 10^5 \text{ cm}^{-1}$ and $1.16 \times 10^5 \text{ cm}^{-1}$) for SnSe and SnS, which is well-matched with experimental data [53,54]. The highest absorption coefficient value (i.e., 10^5 cm^{-1}) means that these materials go from the visible to the infrared region and behave as good absorbing material. The refractive index, extinction coefficient, reflectivity, and energy loss function variation with frequency are shown in Table 3.

Dielectric constant ($\epsilon(\omega)$) is an essential property of a material. The

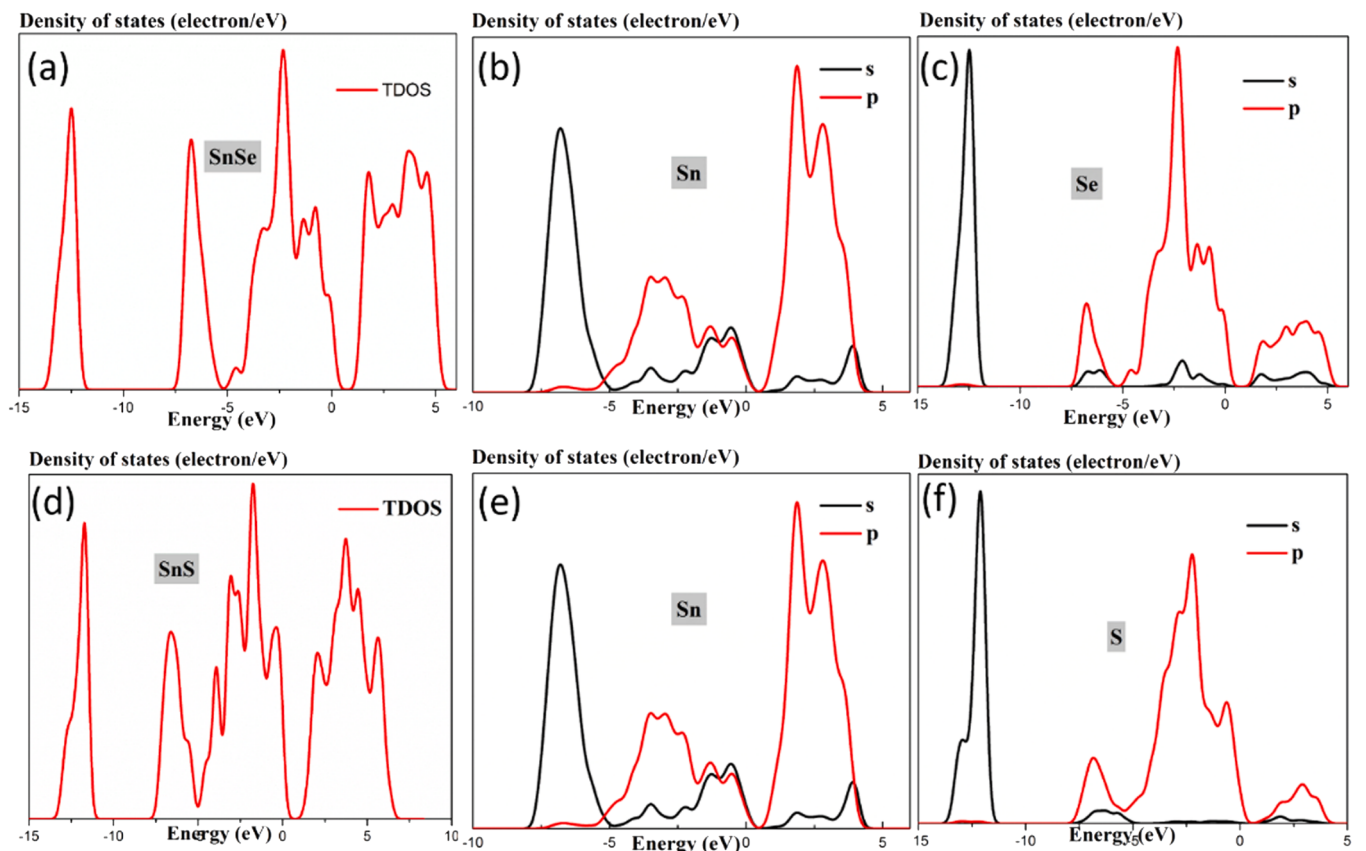


Fig. 4. Total density states and partial density of SnSe and SnS.

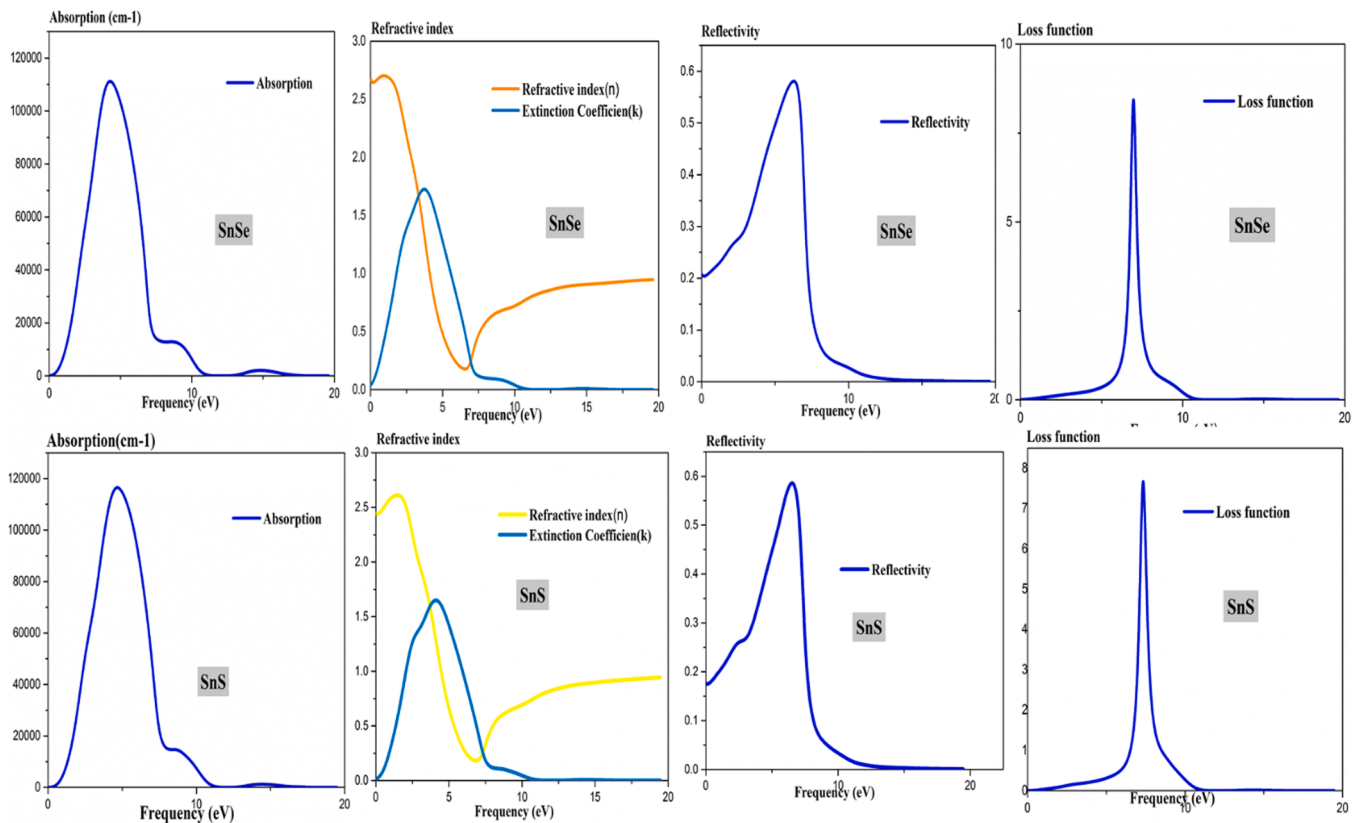


Fig. 5. The frequency-dependent absorption spectra, refractive index, extinction coefficient, reflectivity, and loss function of Sn-monochalcogenides.

Table 3

The absorption coefficient, refractive index, extinction coefficient, reflectivity, and loss function values of Sn-monochalcogenides.

Material	Absorption Coefficient (cm^{-1})	Refractive index (n)	Extinction Coefficient (k)	Reflectivity (eV)	Loss Function (eV)
SnSe	1.11×10^5	2.69	1.72	6.27	6.95
SnS	1.16×10^5	2.61	1.64	6.50	7.66

real part of the dielectric constant ($\epsilon(\omega)$) is used to slow down the speed of light inside the material [41]. Fig. 6 shows the difference in the real components of the $\epsilon(\omega)$ through photon energy. There is free electron gas approximation for the high-frequency scheme $\epsilon(\omega)$ is

$$\epsilon(\omega) = 1 - \frac{\omega_p^2}{\omega^2} \quad (9)$$

In the above equation ω_p is the plasma frequency of the material can be given as follows,

$$\omega_p = \sqrt{\frac{4\pi n e^2}{m}} \quad (10)$$

We have calculated the value $\epsilon(\omega)$ for monolayer and bilayer and correlated it with their bulk counterparts. The curves $\epsilon(\omega)$ for both materials (SnX) are depicted in Fig. 6, which represent several variations to some point. It also illustrates the isotropic response of the material. From here, one can see in the bulk material that the resonance feature is widening due to characteristics of carrier relaxation frequencies and optical transitions rising from an interlayer distance as compared with

their layered structure. At low frequency, we can see the difference in $\epsilon(\omega)$ near to absorption edge and the value $\epsilon(\omega)$ is typically smaller as compared with bulk. For monolayer and bilayer SnSe, the value $\epsilon(\omega)$ is 5.5–7.2 eV, and similarly, for SnS, the value $\epsilon(\omega)$ is associated with the number of layers. It shows the isotropic behavior of the SnSe and SnS. At high frequency, the $\epsilon(\omega)$ monochalcogenides show a constant value; for SnSe, its value is 0.69 eV, and for SnS, it is 0.79 eV. At $\text{Re}(\epsilon) = 0$ the plasma frequency (ω_p) of SnSe and SnS can be predicted by using computational dielectric function. The calculated values are 15–20 eV, comparable with experimental data [55].

For monolayer, bilayer, and bulk, the peaks become sharper as the number of layers decreases. This is because of the deviation of the mutual density of states for hinder points of $E_f(k) - E_i(k)$. The values of the dielectric constant of three forms of materials are listed in Table 4.

4. Conclusions

In short, we have performed a theoretical calculation on tin monochalcogenides' electronic and optical properties. To explore the

Table 4

The calculated result of the real part of dielectric constant and plasmon frequency for monolayer, bilayer, and bulk tin mono-chalcogenides at high energy.

	Monolayer		Bilayer		Bulk	
	ϵ^0_r	ω_p	ϵ^0_r	ω_p	ϵ^0_r	ω_p
SnSe	5.5	19.62	7.2	19.62	8.7	19.7
SnS	4.1	19.54	6	19.54	10	19.63

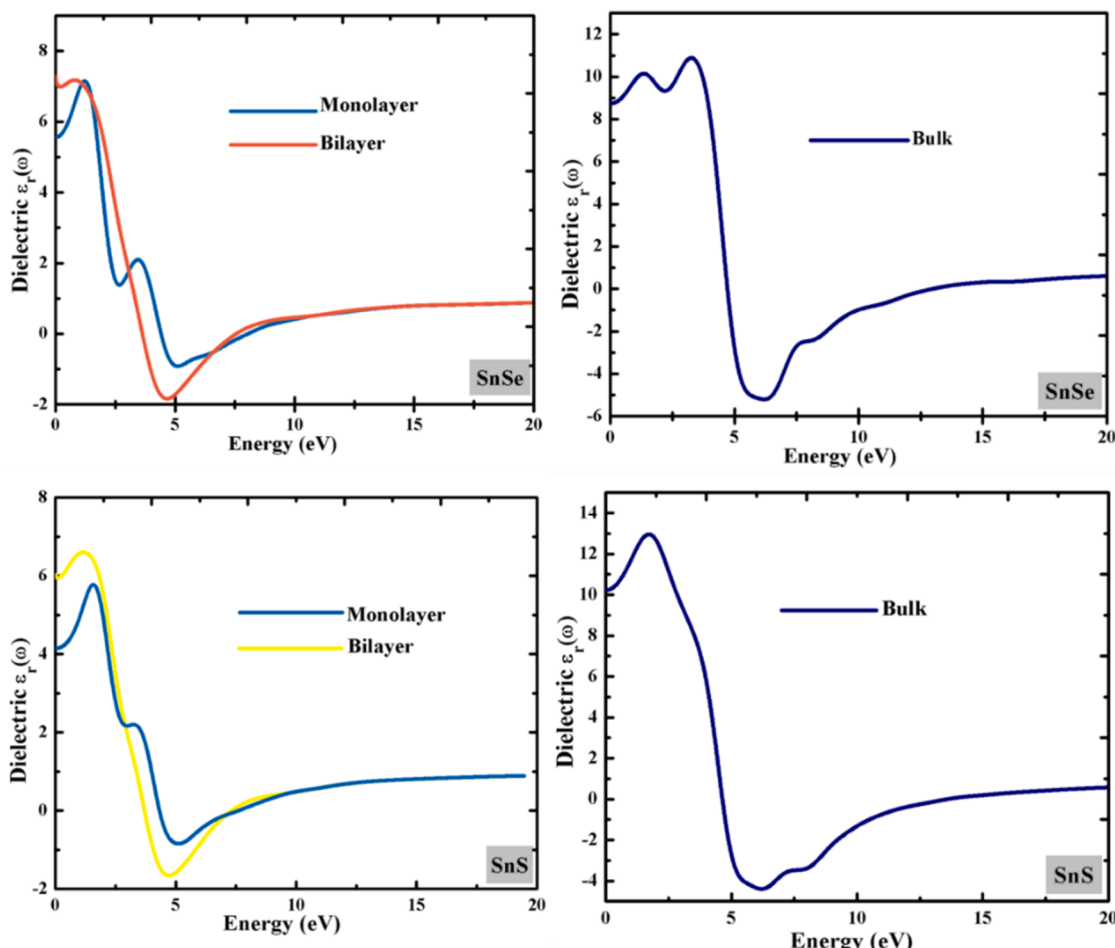


Fig. 6. Comparison of the real part of $\epsilon_r(\omega)$ of tin mono-chalcogenides (monolayer, bilayer) with bulk form.

consequence of dimensionality, the calculation is carried out on the three forms of SnS and SnSe (i.e., monolayer, bilayer, and bulk). The theoretical calculation is achieved using the CASTEP density functional theory with GGA PBE approximation. The optimized lattice parameters of tin mono chalcogenides are comparable with experimental results. The slight difference in lattice parameters of these materials guarantees the tunable optoelectronic properties by adding alloys. From the DFT calculations, the bandgap investigated from monolayer to bulk covers an extensive array of bandgap energy values ranging between 0.5 and 1.25 eV. The dielectric constant for both monochalcogenides increases as the number of layer increase. In the case of SnSe, the dielectric constant from monolayer to bilayer is 5.5 to 7.2 eV; in the SnS, it is 4.1 to 6 eV. The increase of dielectric as the thickness increase shows the material is isotropic. This work demonstrates that controlling the layer number of monochalcogenides can bring about remarkable optical and electronic properties. We theoretically predict symmetry disorder and lower dimensionality by changing layer thickness. These results will open a new window for fabricating high-performance optoelectronics devices, lithium-ion batteries, and catalysis.

Declaration of Competing Interest

The authors declare that they have no known competing financial interests or personal relationships that could have appeared to influence the work reported in this paper.

Acknowledgments

This work was supported by the National Natural Science Foundation of China (2311023).

References

- [1] C. Chang, et al., 3D charge and 2D phonon transports leading to high out-of-plane $\langle ZT \rangle$ in n-type SnSe crystals, *Science* 360 (6390) (2018) 778.
- [2] G. Tan, L.-D. Zhao, M.G. Kanatzidis, Rationally Designing High-Performance Bulk Thermoelectric Materials, *Chemical Reviews* 116 (19) (2016) 12123–12149.
- [3] A. Banik, S. Roychowdhury, K. Biswas, The journey of tin chalcogenides towards high-performance thermoelectrics and topological materials, *Chemical Communications* 54 (50) (2018) 6573–6590.
- [4] G. Qin, et al., Diverse anisotropy of phonon transport in two-dimensional group IV-VI compounds: A comparative study, *Nanoscale* 8 (21) (2016) 11306–11319.
- [5] W. Yu, et al., Atomically thin binary V-V compound semiconductor: a first-principles study, *Journal of Materials Chemistry C* 4 (27) (2016) 6581–6587.
- [6] H. Zheng, et al., Monolayer II-VI semiconductors: A first-principles prediction, *Physical Review B* 92 (11) (2015), 115307.
- [7] H. Şahin, et al., Monolayer honeycomb structures of group-IV elements and III-V binary compounds: First-principles calculations, *Physical Review B* 80 (15) (2009), 155453.
- [8] T. Suzuki, Theoretical discovery of stable structures of group III-V monolayers: The materials for semiconductor devices, *Applied Physics Letters* 107 (21) (2015), 213105.
- [9] S. Lebegue, O. Eriksson, Electronic structure of two-dimensional crystals from ab initio theory, *Physical Review B* 79 (11) (2009), 115409.
- [10] M. Naguib, et al., Two-Dimensional Transition Metal Carbides, *ACS Nano* 6 (2) (2012) 1322–1331.
- [11] Y. Xie, P.R.C. Kent, Hybrid density functional study of structural and electronic properties of functionalized $Ti_{n+1}X_n$ (\$X=\text{Ge}\$, N) monolayers, *Physical Review B* 87 (23) (2013), 235441.
- [12] Q. Hu, et al., MXene: A New Family of Promising Hydrogen Storage Medium, *The Journal of Physical Chemistry A* 117 (51) (2013) 14253–14260.
- [13] H.L. Zhuang, R.G. Hennig, Computational identification of single-layer CdO for electronic and optical applications, *Applied Physics Letters* 103 (21) (2013), 212102.
- [14] R. Ma, T. Sasaki, Nanosheets of Oxides and Hydroxides: Ultimate 2D Charge-Bearing Functional Crystallites, *Advanced Materials* 22 (45) (2010) 5082–5104.
- [15] K.F. Mak, J. Shan, Photonics and optoelectronics of 2D semiconductor transition metal dichalcogenides, *Nature Photonics* 10 (4) (2016) 216–226.
- [16] H. Wang, et al., Physical and chemical tuning of two-dimensional transition metal dichalcogenides, *Chemical Society Reviews* 44 (9) (2015) 2664–2680.
- [17] D. Voiry, J. Yang, M. Chhowalla, Recent Strategies for Improving the Catalytic Activity of 2D TMD Nanosheets Toward the Hydrogen Evolution Reaction, *Advanced Materials* 28 (29) (2016) 6197–6206.
- [18] Q. Lu, et al., 2D Transition-Metal-Dichalcogenide-Nanosheet-Based Composites for Photocatalytic and Electrocatalytic Hydrogen Evolution Reactions, *Advanced Materials* 28 (10) (2016) 1917–1933.
- [19] K. Khan, et al., Recent developments in emerging two-dimensional materials and their applications, *Journal of Materials Chemistry C* 8 (2) (2020) 387–440.
- [20] D.-H. Lee, C.-M. Park, Tin Selenides with Layered Crystal Structures for Li-Ion Batteries: Interesting Phase Change Mechanisms and Outstanding Electrochemical Behaviors, *ACS Applied Materials & Interfaces* 9 (18) (2017) 15439–15448.
- [21] H. Kim, et al., Nanocomb Architecture Design Using Germanium Selenide as High-Performance Lithium Storage Material, *Chemistry of Materials* 28 (17) (2016) 6146–6151.
- [22] W. Li, X. Sun, Y. Yu, Ge-Si, Sn-Based Anode Materials for Lithium-Ion Batteries: From Structure Design to Electrochemical Performance, *Small Methods*, 1 (3) (2017), 1600037.
- [23] P. Wu, et al., Crystal structure of high-performance thermoelectric materials by high resolution neutron powder diffraction, *Physica B: Condensed Matter* 551 (2018) 64–68.
- [24] M.A. Franzman, et al., Solution-Phase Synthesis of SnSe Nanocrystals for Use in Solar Cells, *Journal of the American Chemical Society* 132 (12) (2010) 4060–4061.
- [25] L.C. Gomes, A. Carvalho, Phosphorene analogues: Isoelectronic two-dimensional group-IV monochalcogenides with orthorhombic structure, *Physical Review B* 92 (8) (2015), 085406.
- [26] I. Lignos, et al., Synthesis of Cesium Lead Halide Perovskite Nanocrystals in a Droplet-Based Microfluidic Platform: Fast Parametric Space Mapping, *Nano Letters* 16 (3) (2016) 1869–1877.
- [27] J.A. Hernandez, et al., Thermoelectric properties of SnSe nanowires with different diameters, *Scientific Reports* 8 (1) (2018) 11966.
- [28] K. Peng, et al., Broad temperature plateau for high Z.T.s in heavily doped p-type SnSe single crystals, *Energy & Environmental Science* 9 (2) (2016) 454–460.
- [29] V.R. Minnam Reddy, et al., Perspectives on SnSe-based thin film solar cells: a comprehensive review, *Journal of Materials Science: Materials in Electronics* 27 (6) (2016) 5491–5508.
- [30] A.K. Singh, R.G. Hennig, Computational prediction of two-dimensional group-IV mono-chalcogenides, *Applied Physics Letters* 105 (4) (2014), 042103.
- [31] L. Xu, et al., Electronic and optical properties of the monolayer group-IV monochalcogenides \$MX_2\$ (\$M=\text{Ge}\$, \$\phantom{\rule{4pt}{0ex}}\text{Sn}\$; \$X=\text{S}\$, \$\phantom{\rule{4pt}{0ex}}\text{Se}\$, \$\phantom{\rule{4pt}{0ex}}\text{Te}\$), *Physical Review B* 95 (23) (2017), 235434.
- [32] T.V. Vu, et al., Enhancement of monolayer SnSe light absorption by strain engineering: A DFT calculation, *Chemical Physics* 521 (2019) 5–13.
- [33] M.D. Segall, et al., First-principles simulation: ideas, illustrations and the CASTEP code, *Journal of Physics: Condensed Matter* 14 (11) (2002) 2717–2744.
- [34] J.P. Perdew, K. Burke, M. Ernzerhof, Generalized Gradient Approximation Made Simple, *Physical Review Letters* 77 (18) (1996) 3865–3868.
- [35] T.H. Fischer, J. Almlöf, General methods for geometry and wave function optimization, *The Journal of Physical Chemistry* 96 (24) (1992) 9768–9774.
- [36] H.J. Monkhorst, J.D. Pack, Special points for Brillouin-zone integrations, *Physical Review B* 13 (12) (1976) 5188–5192.
- [37] The high temperature structure of β -Sn and β -SnSe and the B16-to-B33 type λ -transition path, *Zeitschrift für Kristallographie, Crystalline Materials*, 1981, p. 143.
- [38] L. Ehm, et al., Pressure-induced structural phase transition in the IV-VI semiconductor SnS, *Journal of Physics: Condensed Matter* 16 (21) (2004) 3545–3554.
- [39] S. Song, et al., Systematically Optimized Bilayered Electron Transport Layer for Highly Efficient Planar Perovskite Solar Cells ($\eta = 21.1\%$), 2, *ACS Energy Letters*, 2017, pp. 2667–2673.
- [40] S. Alptekin, M. Durandurdu, Formation of a Cmcm phase in SnS at high pressure; an ab initio constant pressure study, *Solid State Communications* 150 (17) (2010) 870–874.
- [41] P.A. Fernandes, et al., Thermodynamic pathway for the formation of SnSe and SnSe₂ polycrystalline thin films by selenization of metal precursors, *CrystEngComm* 15 (47) (2013) 10278–10286.
- [42] B.D. Malone, E. Kaxiras, Quasiparticle band structures and interface physics of SnS and GeS, *Physical Review B* 87 (24) (2013), 245312.
- [43] A.S. Rodin, A. Carvalho, A.H. Castro Neto, Excitons in anisotropic two-dimensional semiconducting crystals, *Physical Review B* 90 (7) (2014), 075429.
- [44] F. Hüser, T. Olsen, K.S. Thygesen, G.W. Quasiparticle, calculations for solids, molecules, and two-dimensional materials, *Physical Review B* 87 (23) (2013), 235132.
- [45] R.W. Godby, P. Garcia-González, Self-Consistent GW Calculations of the Total Energy of Electron Systems, in: *APS March Meeting Abstracts*, 2000.
- [46] K. Kośmider, J.W. González, J. Fernández-Rossier, Large spin splitting in the conduction band of transition metal dichalcogenide monolayers, *Physical Review B* 88 (24) (2013), 245436.
- [47] I. Lefebvre, et al., Electronic structure of tin monochalcogenides from SnO to SnTe, *Physical Review B* 58 (4) (1998) 1896–1906.
- [48] P. Zhang, J. Zhang, J. Gong, Tantalum-based semiconductors for solar water splitting, *Chemical Society Reviews* 43 (13) (2014) 4395–4422.
- [49] M. Parenteau, C. Carbone, Influence of temperature and pressure on the electronic transitions in SnS and SnSe semiconductors, *Physical Review B* 41 (8) (1990) 5227–5234.
- [50] J.D. Wiley, et al., Reflectivity of single-crystal GeS from 0.1 to 30 eV, *Physical Review B* 14 (2) (1976) 697–701.
- [51] S. Logothetidis, H.M. Polatoglou, Ellipsometric studies of the dielectric function of SnSe and a simple model of the electronic structure and the bonds of the orthorhombic IV-VI compounds, *Physical Review B* 36 (14) (1987) 7491–7499.

- [52] J. Yang, et al., Outstanding thermoelectric performances for both p- and n-type SnSe from first-principles study, *Journal of Alloys and Compounds* 644 (2015) 615–620.
- [53] K. Assili, K. Alouani, X. Vilanova, Structural and optical properties of tin (II) sulfide thin films deposited using organophosphorus precursor (Ph₃PS), *Semiconductor Science and Technology* 32 (2) (2017), 025002.
- [54] V.R. Solanki, et al., Structural and optical properties of tin selenide thin films prepared by chemical bath deposition method, in: *AIP Conference Proceedings* 1837, 2017, 040019.
- [55] R. Eymard, A. Otto, Optical and electron-energy-loss spectroscopy of GeS, GeSe, SnS, and SnSe single crystals, *Physical Review B* 16 (4) (1977) 1616–1623.